Beyond the staple motif: a new order at the thiolate–gold interface†

Guoxiang Hu,[a] Rongchao Jin[b] and De-en Jiang*[a]

Staple motifs in the form of −RS(AuSR)$_x$− (x = 1, 2, 3, *etc.*) are the most common structural feature at the interface of the thiolate-protected gold nanoclusters, Au$_n$(SR)$_m$. However, the recently solved structure of Au$_{92}$(SR)$_{44}$, in which the facets of the Au$_{84}$ core are protected mainly by the bridging thiolates, challenges the staple hypothesis. Herein, we explore the surface sensitivity of the thiolate–gold interface from first principles density functional theory. We find that the interfacial structures of thiolates on gold are surface sensitive: while a staple motif (such as −RS–Au–SR−) is preferred on Au(111), a bridging motif (−RS−) is preferred on Au(100) and Au(110). We show that this surface sensitivity is closely related to the coordination number of the surface Au atom on the different surfaces. We further confirm the preference of the bridging motif for self-assembled monolayers of two different ligands (methylthiolate and 4-*tert*-butyl-benzenethiolate) on Au(100). With this surface sensitivity, we categorize the structure-known Au$_n$(SR)$_m$ clusters into three groups: (1) no bridging; (2) ambiguous bridging; (3) distinct bridging. We further employ the surface sensitivity of the thiolate–Au interface to predict the protecting motifs of face-centered cubic (fcc) gold nanoparticles of different shapes. Our study provides a unifying view of the Au$_n$(SR)$_m$ structures with guidelines for structure predictions for larger Au$_n$(SR)$_m$ clusters of a fcc core.

Introduction

Thiolate-protected gold nanoclusters with the formula Au$_n$(SR)$_m$ have received considerable attention over the past decade owing to their unique structures and physicochemical properties that are not seen in larger gold nanoparticles or bulk gold.[1–10] Their potential applications range from catalysis to bioimaging and protein labeling.[11–16] To date, total structures of about 20 such clusters ranging from Au$_{18}$(SC$_6$H$_{11}$)$_{14}$ to Au$_{133}$(SPh-*p*-^{t}Bu)$_{52}$ have been successfully solved *via* single-crystal X-ray crystallography.[17–38] The structural determinations of these clusters provide profound insights into the thiolate–gold interface and bonding, which are key to the formation and stability of the thiolate-protected gold nanoclusters. Among these clusters, Au$_{102}$(SPh-*p*-COOH)$_{44}$ was the first one to be crystallized and characterized; the 44 thiolate groups of the cluster form 19 RS–Au–SR motifs and 2 RS–Au–SR–Au–SR motifs on the cluster surface, which were termed the staple motif.[35] Similar RS–Au–SR motifs were also found in self-assembled monolayers (SAMs) on Au(111) with both

experimental and theoretical studies.[39–41] These reports highlight the importance of the staple motifs at the thiolate–gold interface; it was hence hypothesized that the staple motifs are preferred at the thiolate–gold interface than the isolated or bridging thiolate (−RS−) group. Computationally, the preference of the staple motif over the bridging thiolate was demonstrated on Au(111) and small gold nanoclusters such as Au$_{38}$.[42]

The staple hypothesis has been successfully applied to predict structures for Au$_n$(SR)$_m$ clusters of known compositions and confirmed in subsequently reported structures. For example, Akola *et al.* proposed a structure model for Au$_{25}$(SR)$_{18}$$^-$,[43] in which an icosahedral Au$_{13}$-core is protected by 6 dimeric staple motifs, which was confirmed independently by two experimental research groups.[22,23] Likewise, Pei *et al.* and Aikens *et al.* have predicted the structure of Au$_{38}$(SR)$_{24}$ to possess a face-fused bi-icosahedral Au$_{23}$ protected by six dimeric and three monomeric staple motifs,[44,45] which was again confirmed in the experimental crystal structure.[31]

As the dominance of the staple motif began to take root in our thinking of the thiolate–gold interface, the line between the staple motif and the bridging thiolate has become blurred in some reported structures, including Au$_{36}$(SPh-*p*-^{t}Bu)$_{24}$,[28] Au$_{28}$(SPh-*p*-^{t}Bu)$_{20}$,[24] and [Au$_{23}$(S-*c*-C$_6$H$_{11}$)$_{16}$]$^-$.[19] For example, the structure of Au$_{36}$(SPh-*p*-^{t}Bu)$_{24}$ can be viewed to have an fcc Au$_{28}$ kernel protected by 4 dimeric staple motifs on 4 Au(111) facets and 12 bridging motifs on 6 Au(100) facets, or

^{a}*Department of Chemistry, University of California, Riverside, California 92521, USA. E-mail: djiang@ucr.edu*
^{b}*Department of Chemistry, Carnegie Mellon University, Pittsburgh, Pennsylvania 15213, USA*

alternatively, as a Au_{20} kernel protected by 4 "regular" dimeric staple motifs and additional 4 "distorted" dimeric staple motifs.[30,46] Likewise, this ambiguity is also manifested in $[Au_{23}(S\text{-}c\text{-}C_6H_{11})_{16}]^-$ and $Au_{28}(SPh\text{-}p\text{-}^tBu)_{20}$.[47] Due to this duality in viewing the gold–thiolate interface, the staple hypothesis has been challenged but survived.

The recently solved structure of $Au_{92}(SPh\text{-}p\text{-}^tBu)_{44}$,[34] however, challenges the staple hypothesis to the fullest extent and demands a rethinking of the thiolate–gold interface, because here, there is no ambiguity. $Au_{92}(SPh\text{-}p\text{-}^tBu)_{44}$ has a highly regular fcc Au_{84} kernel with 16-gold-atom (001) facets and 12-gold-atom (100) and (010) facets, which are distinctly and clearly covered by the bridging thiolates.[34] This new structure raises the key question about the surface sensitivity of the thiolate–gold interface. Previously, the preference of the staple motif was demonstrated only for the Au(111) surface. It is therefore of great importance to examine the energetic stability of the staple *vs.* bridging mode at the gold–thiolate interface for other surfaces such as (100) and (110). In addition, the structure of $Au_{92}(SPh\text{-}p\text{-}^tBu)_{44}$ now gives more weight to the view of the bridging thiolate for structures where ambiguity existed.

To understand the bridging motifs at the interface of the thiolate-protected gold nanoclusters in particular and to provide guidelines for future structure predictions in general, herein, we study the surface sensitivity of the thiolate–gold interface with three low-Miller-index surfaces of gold including Au(111), Au(100), and Au(110) from first-principles density functional theory (DFT). We then explain the energetic trend found. Next, we leverage the surface sensitivity to categorize the existing clusters into three groups: (1) no bridging, (2) ambiguous bridging, and (3) distinct bridging. Furthermore, we employ the surface sensitivity to predict the protecting motifs of fcc gold nanoparticles (smaller than 3 nm) with different shapes.

Results and discussion

Bridging and staple motifs on Au(111), Au(100), and Au(110)

To examine the surface sensitivity of the thiolate–gold interface, we use methylthiolate (MT) as an example. We tested all the possible adsorption sites on the three surfaces: top, bridge, fcc, and hcp sites on Au(111); top, bridge, and hollow sites on Au(100); top, long bridge, short bridge, 3-fold hollow, and 4-fold hollow sites on Au(110). By comparing the binding energies (see Tables S1–S3 of the ESI† for details of the comparison), we found that the bridge sites are the most stable adsorption sites for MT on all the three surfaces (Fig. 1), where each MT binds to two neighboring surface gold atoms. This mode is also found at the Au–thiolate–Au interfaces of molecular nanowires.[48,49]

We next examine the staple motif (CH_3S–Au_{adatom}–SCH_3) on the Au surfaces. Fig. 2 shows the optimized structure of the most stable form of the staple motif on Au(111).[39] Fig. 3 shows three types of staple motifs on Au(100) of comparable energy:
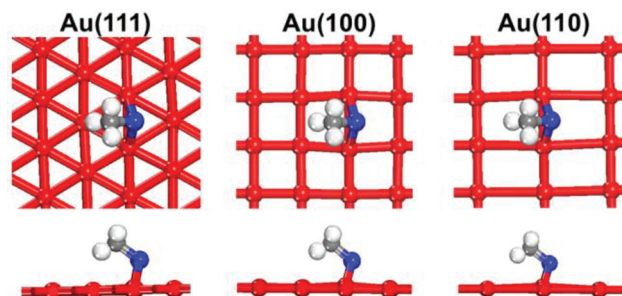

Fig. 1 Top view (upper panel) and side view (lower panel) of the optimized structures for bridging methylthiolate on Au(111), Au(100), and Au(110) surfaces. Only the topmost surface layer is shown. Au, red; S, blue; C, grey; H, white.
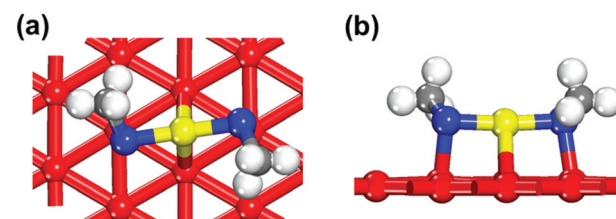

Fig. 2 Top view (a) and side view (b) of the optimized structures for the CH_3S–Au_{adatom}–SCH_3 staple motif on Au(111). Only the topmost surface layer is shown. Au_{adatom}, yellow; other Au, red; S, blue; C, grey; H, white.

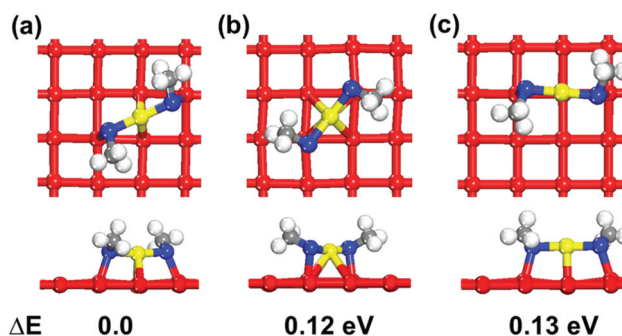**Fig. 3** Top view (upper panel) and side view (lower panel) of the optimized structures for the staple motifs on Au(100). (a) Au_{adatom} at the bridging site; (b) Au_{adatom} at the hollow site; (c) Au_{adatom} at the top site. Only the topmost surface layer is shown. Au_{adatom}, yellow; other Au, red; S, blue; C, grey; H, white. Differences of the total energies (ΔE) based on a four-layer slab in (4 × 4) lateral cells are listed for comparison.

the most stable structure (Fig. 3a) has the Au adatom at the bridge site and the staple motif lays diagonally across two neighboring Au squares; the second type (Fig. 3b) has the Au adatom at the hollow site and the staple motif lays diagonally across one Au square; the third type (Fig. 3c) has the Au adatom at the top site and the staple motif lays on top of the long edge of two neighboring Au squares. On Au(110), we explored five types of staple motifs (Fig. 4). The first three (Fig. 4a–c) are close in energy. In the most stable structure (Fig. 4a), the Au adatom is at the top site and the staple motif
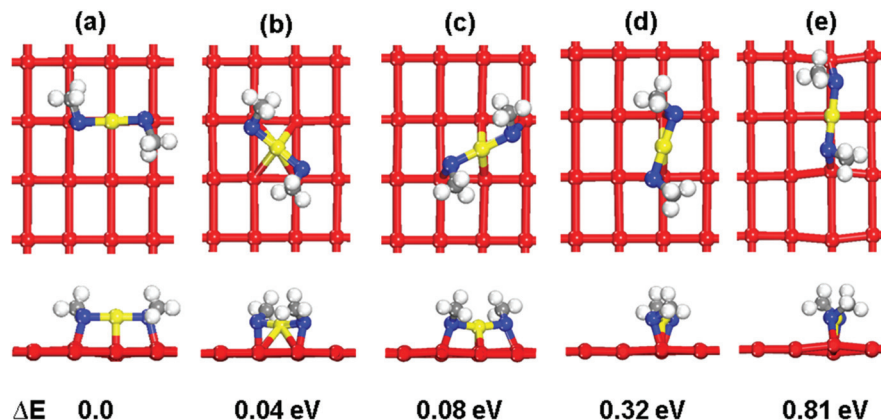
Fig. 4 Top view (upper panel) and side view (lower panel) of the optimized structures for the staple motifs on Au(110). (a) and (e) Au_{adatom} at the top site; (b) Au_{adatom} at the rectangular hollow site; (c) and (d) Au_{adatom} at the long bridge site. Only the topmost surface layer is shown. Au_{adatom}, yellow; other Au, red; S, blue; C, grey; H, white. Differences of the total energies (ΔE) based on a six-layer slab in (3×4) lateral cells are listed for comparison.

lies on top of two neighboring short Au–Au edges. In the second type (Fig. 4b), the Au adatom is at the hollow site and the staple motif lies diagonally cross the Au rectangle. In the third type (Fig. 4c), the Au adatom is at the long-bridge site and the staple motif lies diagonally across two neighboring Au rectangles sharing the long edge.

Fig. 5 shows the comparison of the binding energies per thiolate for the most stable modes of the bridging and staple motifs on the three Au surfaces. One can see that although a staple motif is preferred on Au(111), a bridging motif is preferred on Au(100) and Au(110). Clearly, the binding mode of the thiolate on Au is surface sensitive. From Au(111) to Au(100) to Au(110), the thiolate group binding is stronger with Au for both the staple motif and the bridging motif, but apparently the increase is more dramatic for the bridging motif, especially

from Au(111) to Au(100). This is the key reason for the surface sensitivity of the binding motif.

To understand the increasing binding energies for the bridging motif, Table 1 lists the Au–S distance and the partial charge on the Au that binds to S, together with the Au–Au coordination number of the different surfaces. One can see that the increasing binding energies from (111) to (100) to (110) correlate well with the shortening Au–S distance and the increasing charge transfer from S to Au. This trend can be well explained by the coordination numbers of the surface Au atoms, which decreases from 9 to 8 to 7 for Au(111), Au(100), and Au(110), respectively. Low-coordinate Au atoms are more reactive and therefore have stronger interactions with the thiolate group; more so for the bridging thiolate than for the thiolate in the staple motif.

To further confirm the binding mode of the thiolate on Au(100), we studied SAMs on Au(100) with bridging and staple motifs. As shown in Fig. 6, the sulfur overlayer has a coverage of 50%, and the overall patterning symmetry is $c(2 \times 2)$. For the bridging motif, one thiolate covers two Au atoms at the bridging site (Fig. 6a), while for the staple motif, with the Au adatom at the bridge site, two thiolates cover diagonally across two neighboring Au squares (Fig. 6b). In this case, we find that the binding energies per thiolate of the bridging and staple motifs are −2.35 eV and −1.89 eV, respectively. Clearly, SAMs on Au(100) with the bridging motif are more stable than the
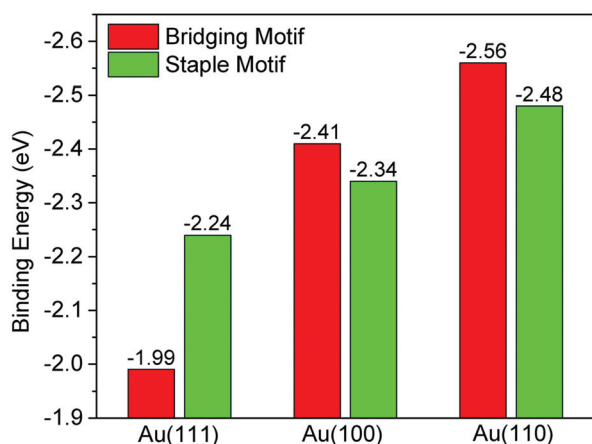

Fig. 5 Comparison of binding energies per methylthiolate for the most stable modes of the bridging and staple motifs on the three Au surfaces. The coverages are one motif per lateral cell of (4×4) for Au(111), (4×4) for Au(100), and (3×4) for Au(110).

Table 1 Au–S bond lengths (r_{Au-S}) of the bridging methylthiolate, Bader charges on the Au atoms bonded to S of bridging methylthiolate, and coordination numbers of the surface Au atoms (C.N.) on each surface

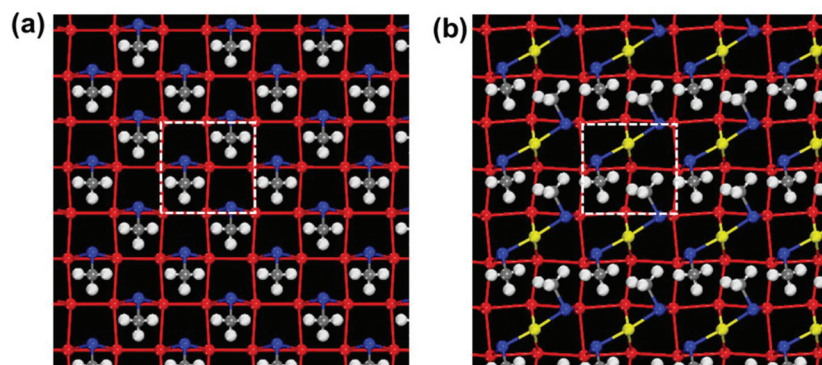|	Au(111)	Au(100)	Au(110)
r_{Au-S}/Å	2.475	2.428	2.416
Bader charge (Au)/$|e|$	+0.049	+0.060	+0.068
C.N. (Au–Au)	9	8	7

Fig. 6 Top views of self-assembled monolayers of methylthiolate (MT) on Au(100): (a) based on the bridging motif; (b) based on the staple motif. The dashed line indicates the unit cell; in both cases, coverage is at 5.75 MT nm^{-2}. Only the topmost surface layer is shown. Au$_{adatom}$, yellow; other Au, red; S, blue; C, grey; H, white.

staple motif. In addition, we replaced the MT with the experimental ligand 4-*tert*-butylbenzenethiolate (TBBT), and considered the van der Waals (vdW) interactions between the ligands. The same trend was found. With a coverage of 25%, the binding energy per TBBT of the bridging motif is −3.01 eV, which is 0.48 eV lower than the staple motif (−2.53 eV). All these observations indicate that the bridging motif rather than the staple motif is preferred on Au(100). Of course, the types of thiolate ligands are more than just MT and TBBT. Because the energetic difference between the bridging and staple motifs is small as shown in Fig. 5 for Au(100), one can expect that the substituent effects (such as electron-drawing with fluorinated thiols, water-soluble ones with glutathione, *etc.*) may affect the interfacial ligand bonding. We hope to further explore them in the future.

Categorizing thiolate-protected gold nanoclusters

The surface sensitivity of the gold–thiolate interface as shown in Fig. 5 can now explain the existence of the bridging motifs

in some Au$_n$(SR)$_m$ clusters. Given this insight, it is necessary to view the existing Au$_n$(SR)$_m$ clusters from the geometry and facet of their cores. Our analysis of the surface sensitivity is based on the fcc geometry, while many Au$_n$(SR)$_m$ clusters have different core geometries. So we will first categorize all the existing thiolate-protected gold nanoclusters according to their interfacial motifs and then correlate them to the core geometry.

We found that all the reported Au$_n$(SR)$_m$ clusters can be summarized into three groups based on their protecting motifs (Table 2): (1) no bridging, *i.e.*, having staple motifs only; (2) ambiguous bridging, *i.e.*, having bridging motifs that are of the ambiguous type only, in addition to staple motifs; (3) distinct bridging, *i.e.*, having distinct bridging motifs, in addition to staple motifs and ambiguous bridging (if any). Table 2 shows that Au$_n$(SR)$_m$ clusters with non-fcc cores, including icosahedral (Ic), marks decahedral (M-Dh), and hexagonal close packing (hcp), have staple motifs only and no bridging thiolates at the interface. A common structural feature of these cores is the dominance of the Au$_3$ triangles on

Table 2 Categorizing thiolate-protected gold nanoclusters into three groups: "no bridging", "ambiguous bridging", and "distinct bridging"

Category	Cluster	Kernel	Protecting motifs
No bridging	Au$_{18}$(SR)$_{14}$	hcp-based Au$_9$	Au$_4$(SR)$_5$ + Au$_2$(SR)$_3$ + 3 Au(SR)$_2$ [17]
	Au$_{20}$(SR)$_{16}$	Bitetrahedral Au$_7$	Au$_8$(SR)$_8$ + Au$_3$(SR)$_4$ + 2 Au(SR)$_2$ [18]
	Au$_{24}$(SR)$_{20}$	Bitetrahedral Au$_8$	4 Au$_4$(SR)$_5$ [21]
	Au$_{25}$(SR)$_{18}$$^{-1/0}$	Ic-based Au$_{13}$	6 Au$_2$(SR)$_3$ [22,23]
	Au$_{30}$(SR)$_{18}$	hcp-based Au$_{18}$	6 Au$_2$(SR)$_3$ [27]
	Au$_{38}$(SR)$_{24}$^{a}	Ic-based Au$_{23}$	6 Au$_2$(SR)$_3$ + 3 Au(SR)$_2$ [31]
	Au$_{102}$(SR)$_{44}$	M-Dh-based Au$_{79}$	2 Au$_2$(SR)$_3$ + 19 Au(SR)$_2$ [35]
	Au$_{130}$(SR)$_{50}$	M-Dh-based Au$_{105}$	25 Au(SR)$_2$ [36]
	Au$_{133}$(SR)$_{52}$	Ic-based Au$_{107}$	26 Au(SR)$_2$ [37,38]
Ambiguous bridging	Au$_{23}$(SR)$_{16}$$^-$	fcc-based Au$_{15}$	2 Au$_3$(SR)$_4$ + 2 Au(SR)$_2$ + 4 SR [19]
	Au$_{28}$(SR)$_{20}$^{b}	fcc-based Au$_{20}$	4 Au$_2$(SR)$_3$ + 8 SR [24]
	Au$_{36}$(SR)$_{24}$	fcc-based Au$_{28}$	4 Au$_2$(SR)$_3$ + 12 SR [28]
	Au$_{40}$(SR)$_{24}$	fcc-based Au$_{34}$	6 Au(SR)$_2$ + 12 SR [33,50]
	Au$_{44}$(SR)$_{28}$	fcc-based Au$_{36}$	4 Au$_2$(SR)$_3$ + 16 SR [51]
	Au$_{52}$(SR)$_{32}$	fcc-based Au$_{44}$	4 Au$_2$(SR)$_3$ + 20 SR [33,51]
Distinct bridging	Au$_{92}$(SR)$_{44}$	fcc-based Au$_{84}$	8 Au(SR)$_2$ + 28 SR [34]

^{a} Au$_{38}$(SR)$_{24}$ has two isomers: Q and T,[31,32] and isomer Q is presented here. ^{b} Au$_{28}$(SR)$_{20}$ has two ligand-induced isomers: Au$_{28}$(SPh-*p*-^{t}Bu)$_{20}$ and Au$_{28}$(S-*c*-C$_6$H$_{11}$)$_{20}$,[24,25] and Au$_{28}$(SPh-*p*-^{t}Bu)$_{20}$ is presented here.[24]
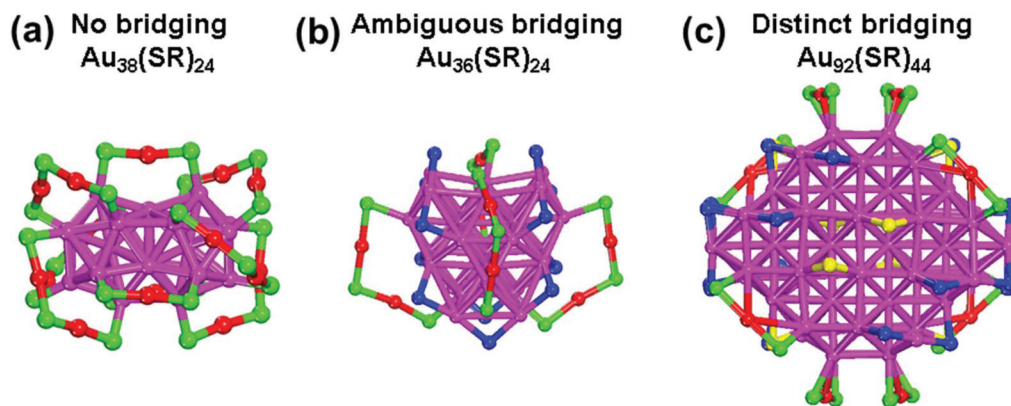
Fig. 7 Typical structures for the three types of $Au_n(SR)_m$ clusters: (a) "no bridging": $Au_{38}(SR)_{24}$, isomer Q; (b) "ambiguous bridging": $Au_{36}(SR)_{24}$; (c) "distinct bridging": $Au_{92}(SR)_{44}$. R-groups are omitted for clarity. Au (kernel), magenta; Au (staple), red; S (staple), green; S (ambiguous bridging), blue; S (distinct bridging), yellow.

the core surface. Similar to Au(111), these triangles prefer the staple motif. This may be why only staple motifs exist at the interface of these clusters with non-fcc cores. Fig. 7a shows the typical structure of "no bridging": $Au_{38}(SR)_{24}$.[31] As one can see, the core surface only exhibits Au_3 triangles, and it is simply protected by the staple motifs.

Table 2 also shows that the clusters belonging to either the ambiguous or distinct bridging type have fcc kernels. This can be due to the fact that fcc-based kernels tend to expose (100) facets which further confirms the surface sensitivity that we found for the surfaces of bulk fcc Au as shown in Fig. 5. Especially for the magic series $Au_{28}(SR)_{20}$, $Au_{36}(SR)_{24}$, $Au_{44}(SR)_{28}$ and $Au_{52}(SR)_{32}$ reported by Jin group, they have 8, 12, 16, and 20 Au_4 {100} squares, respectively, in addition to four {111} facets. Significantly, the surface-protecting modes of these clusters obey the same rules: each {111} facet is protected by one dimeric staple motif, and each {100} square is protected by one bridging motif.[51] Similarly for $Au_{23}(SR)_{16}^-$ and $Au_{40}(SR)_{24}$, all the bridging motifs appear over the squares. These structures are called ambiguous bridging structures because the bridging thiolates can be viewed alternatively as part of the staple motifs with a different core geometry. Fig. 7b shows the typical structure of "ambiguous bridging": $Au_{36}(SR)_{24}$.[28] The ambiguous bridging thiolates are colored with blue. As one can see, these 12 ambiguous bridging motifs can be viewed alternatively as 4 dimeric staple motifs. But our finding of the surface sensitivity supports the view from the bridging thiolate: the core takes a compact fcc geometry, instead of a less ordered and hard-to-describe core as in the view from the staple motif. We think that the bridging-motif view and the staple-motif view in the case of "ambiguous bridging" are like the two sides of a coin; together, they offer a more complete view of the gold–thiolate interface. Previous analysis of the Bader charges on the gold atoms between the bridging thiolates of $Au_{28}(SR)_{20}$ suggested that they resemble the gold atoms in the staple motifs more than the core gold atoms.[25,47]

In the case of $Au_{92}(SR)_{44}$, distinct bridging thiolates are observed on the planar (100) facets because these bridging thiolates (yellow in Fig. 7c) cannot be viewed as part of the staple motifs. One can also see ambiguous bridging thiolates (blue in Fig. 7c) at the edges of the tetragonal $Au_{92}(SR)_{44}$.[34] Although $Au_{92}(SR)_{44}$ is the only member of the "distinct bridging" type, we think that there will be more structures in this category to be discovered. Below, we present predictions of possible structures of this type.

Implications for structure predictions based on the surface sensitivity

Based on the facet sensitivity, we can predict the protecting motifs of fcc gold nanoparticles smaller than 3 nm. "Geometrically ideal" shapes of fcc nanoparticles include cube (terminated completely by {100} surfaces), truncated cube, cuboctahedron, truncated octahedron, and octahedron (terminated completely by {111} surfaces). Here we choose five fcc gold nanoparticles with different shapes, namely, cubic Au_{108}, truncated cubic Au_{171}, cuboctahedral Au_{147}, truncated octahedral Au_{140}, and octahedral Au_{146},[52] and predict their protecting motifs with the facet sensitivity. As shown in Fig. 8, we predict that cores such as cubic Au_{108}, truncated cubic Au_{171}, and cuboctahedral Au_{147} cores will have distinct bridging motifs on their surfaces.

The surface sensitivity we found also has an important implication for a recently proposed structure of $Au_{144}(SR)_{60}$. From their pair-distribution function (PDF) experiment and analysis, Ackerson et al. found that the $Au_{144}(SR)_{60}$ cluster can exist in two different polymorphs; they proposed a decahedral Au_{114} core (Fig. 9) that is different from the popular model of the icosahedral Au_{114} core.[53,54] The proposed Au_{114} core of $Au_{144}(SR)_{60}$ exhibit five (111) facets at the top and another five at the bottom, as well as five (100) facets on the waist. Our finding of the facet sensitivity of the thiolate–gold interface suggests that the planar (100) facets should be protected by the bridging motifs instead of the staple motifs. Therefore, structure prediction of the new $Au_{144}(SR)_{60}$ polymorph based
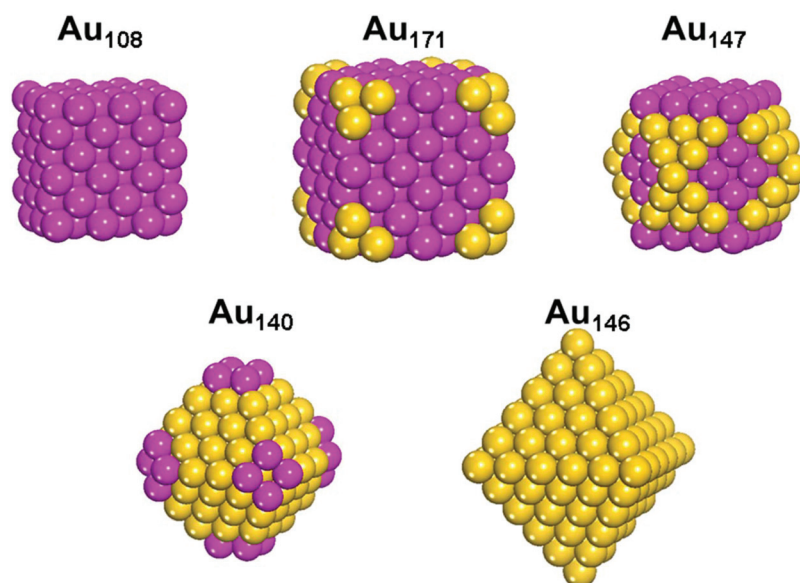
Fig. 8 Five fcc gold nanoparticles with different shapes, namely, cubic Au_{108}, truncated cubic Au_{171}, cuboctahedral Au_{147}, truncated octahedral Au_{140}, and octahedral Au_{146}. The exposing (100) facets are colored with magenta, while the exposing (111) facets are colored with yellow.
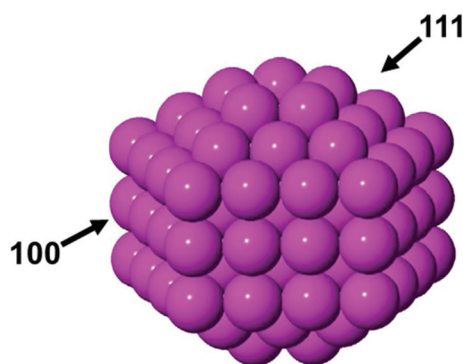

Fig. 9 The proposed Au_{114} kernel of $Au_{144}(SR)_{60}$.

on the decahedral Au_{114} core needs to take into account both the bridging thiolates in addition to the staple motifs.

Conclusions

To shed light on the bridging motifs at the interface of the thiolate-protected gold nanoclusters, we have studied the facet or surface sensitivity of the thiolate–gold interface with three low-Miller-index surfaces of gold, including Au(111), Au(100), and Au(110) with DFT. We found that the interfacial structures of thiolates on gold are surface sensitive: while a staple motif (–RS–Au–SR–) is preferred on Au(111), a bridging motif (–RS–) is preferred on Au(100) and Au(110). The Au(100) surface's preference for the bridging motif is due to the low coordination number of its surface gold atoms and further confirmed for self-assembled monolayers of thiolates on it. The surface

sensitivity allowed us to categorize the structure-known $Au_n(SR)_m$ clusters into three groups: (1) no bridging; (2) ambiguous bridging; (3) distinct bridging. It further enabled us to predict the protecting motifs of face-centered cubic (fcc) gold nanoparticles (smaller than 3 nm) of different shapes.

Computational methods

Periodic DFT calculations were performed by using the Vienna *ab initio* simulation package (VASP).[55] The ion–electron interaction was described using the projector augmented wave (PAW) method.[56] Electron exchange–correlation was represented by the functional of Perdew, Burke and Ernzerhof (PBE) of generalized gradient approximation (GGA).[57] The PBE-GGA functional has been demonstrated to achieve a good balance between accuracy and cost for gold–thiolate systems.[46] A cutoff energy of 400 eV was used for the plane-wave basis set. The calculated Au fcc lattice parameter is 4.169 Å, which agrees reasonably with the experimental value (4.078 Å). The gold surfaces were modeled with four layers of slabs in (4 × 4) lateral cells for Au(111) and Au(100), and six layers of slab in (3 × 4) lateral cells (12.506 Å × 11.791 Å) for Au(110), with 15 Å of vacuum along the *z*-direction. The Brillouin zone was sampled by (3 × 3 × 1) Monkhorst–Pack *k*-point mesh. The top half of the slab was allowed to relax together with the adsorbed thiolates and the convergence threshold for structural optimization was set to be 0.025 eV Å^{-1} in force. Partial atomic charges were obtained using Bader charge analysis as implemented by Henkelman and co-workers.[58] The vdW interactions were included *via* the DFT-D3 method for structural optimizations with the experimental ligand TBBT.[59]

The binding energy of the bridging motif (–RS–) was calculated by

$$E_b = E_{\text{thiol/Au\_slab}} - E_{\text{Au\_slab}} - E_{\text{SR}} \tag{1}$$

where $E_{\text{thiol/Au\_slab}}$, $E_{\text{Au\_slab}}$, and E_{SR} represent the total energy of the adsorbate–substrate system, the total energy of the Au slab, and the energy of one gas phase SR, respectively. The binding energy of the staple motif (–RS–Au–SR–) was calculated by

$$E_b = \frac{1}{2}\left(E_{\text{thiol/Au\_slab}} - E_{\text{Au\_slab}} - 2E_{\text{SR}} - E_{\text{Au}}^{\text{Bulk}}\right) \tag{2}$$

where $E_{\text{Au}}^{\text{Bulk}}$ is the energy of one bulk Au atom. Here, we considered the energy involved in the Au adatom formation needed for the staple motif.[60] A negative value of E_b suggests favorable adsorption.

Acknowledgements

References

1 M. M. Alvarez, J. T. Khoury, T. G. Schaaff, M. N. Shafigullin, I. Vezmar and R. L. Whetten, *J. Phys. Chem. B*, 1997, **101**, 3706–3712.
2 S. Chen, R. S. Ingram, M. J. Hostetler, J. J. Pietron, R. W. Murray, T. G. Schaaff, J. T. Khoury, M. M. Alvarez and R. L. Whetten, *Science*, 1998, **280**, 2098–2101.
3 Y. Negishi, K. Nobusada and T. Tsukuda, *J. Am. Chem. Soc.*, 2005, **127**, 5261–5270.
4 A. S. K. Hashmi and G. J. Hutchings, *Angew. Chem., Int. Ed.*, 2006, **45**, 7896–7936.
5 H. Hakkinen, *Nat. Chem.*, 2012, **4**, 443–455.
6 T. Tsukuda, *Bull. Chem. Soc. Jpn.*, 2012, **85**, 151–168.
7 Y. Pei and X. C. Zeng, *Nanoscale*, 2012, **4**, 4054–4072.
8 H. Qian, M. Zhu, Z. Wu and R. Jin, *Acc. Chem. Res.*, 2012, **45**, 1470–1479.
9 T. Bürgi, *Nanoscale*, 2015, **7**, 15553–15567.
10 R. Jin, C. Zeng, M. Zhou and Y. Chen, *Chem. Rev.*, 2016, **116**, 10346–10413.
11 R. W. Murray, *Chem. Rev.*, 2008, **108**, 2688–2720.
12 R. Jin, *Nanoscale*, 2010, **2**, 343–362.
13 C. J. Ackerson, R. D. Powell and J. F. Hainfeld, *Methods Enzymol.*, 2010, **481**, 195–230.
14 P. Maity, S. Xie, M. Yamauchi and T. Tsukuda, *Nanoscale*, 2012, **4**, 4027–4037.
15 G. Li and R. Jin, *Acc. Chem. Res.*, 2013, **46**, 1749–1758.
16 R. Jin, *Nanoscale*, 2015, **7**, 1549–1565.
17 A. Das, C. Liu, H. Y. Byun, K. Nobusada, S. Zhao, N. Rosi and R. Jin, *Angew. Chem., Int. Ed.*, 2015, **54**, 3140–3144.
18 C. Zeng, C. Liu, Y. Chen, N. L. Rosi and R. Jin, *J. Am. Chem. Soc.*, 2014, **136**, 11922–11925.
19 A. Das, T. Li, K. Nobusada, C. Zeng, N. L. Rosi and R. Jin, *J. Am. Chem. Soc.*, 2013, **135**, 18264–18267.
20 D. Crasto, G. Barcaro, M. Stener, L. Sementa, A. Fortunelli and A. Dass, *J. Am. Chem. Soc.*, 2014, **136**, 14933–14940.
21 A. Das, T. Li, G. Li, K. Nobusada, C. Zeng, N. L. Rosi and R. Jin, *Nanoscale*, 2014, **6**, 6458–6462.
22 M. Zhu, C. M. Aikens, F. J. Hollander, G. C. Schatz and R. Jin, *J. Am. Chem. Soc.*, 2008, **130**, 5883–5885.
23 M. W. Heaven, A. Dass, P. S. White, K. M. Holt and R. W. Murray, *J. Am. Chem. Soc.*, 2008, **130**, 3754–3755.
24 C. Zeng, T. Li, A. Das, N. L. Rosi and R. Jin, *J. Am. Chem. Soc.*, 2013, **135**, 10011–10013.
25 Y. Chen, C. Liu, Q. Tang, C. Zeng, T. Higaki, A. Das, D. E. Jiang, N. L. Rosi and R. Jin, *J. Am. Chem. Soc.*, 2016, **138**, 1482–1485.
26 D. Crasto, S. Malola, G. Brosofsky, A. Dass and H. Hakkinen, *J. Am. Chem. Soc.*, 2014, **136**, 5000–5005.
27 T. Higaki, C. Liu, C. Zeng, R. Jin, Y. Chen, N. L. Rosi and R. Jin, *Angew. Chem., Int. Ed.*, 2016, **55**, 6694–6697.
28 C. Zeng, H. Qian, T. Li, G. Li, N. L. Rosi, B. Yoon, R. N. Barnett, R. L. Whetten, U. Landman and R. Jin, *Angew. Chem., Int. Ed.*, 2012, **124**, 13291–13295.
29 A. Das, C. Liu, C. Zeng, G. Li, T. Li, N. L. Rosi and R. Jin, *J. Phys. Chem. A*, 2014, **118**, 8264–8269.
30 P. R. Nimmala, S. Knoppe, V. R. Jupally, J. H. Delcamp, C. M. Aikens and A. Dass, *J. Phys. Chem. B*, 2014, **118**, 14157–14167.
31 H. Qian, W. T. Eckenhoff, Y. Zhu, T. Pintauer and R. Jin, *J. Am. Chem. Soc.*, 2010, **132**, 8280–8281.
32 S. Tian, Y. Z. Li, M. B. Li, J. Yuan, J. Yang, Z. Wu and R. Jin, *Nat. Commun.*, 2015, **6**, 8667.
33 C. Zeng, Y. Chen, C. Liu, K. Nobusada, N. L. Rosi and R. Jin, *Sci. Adv.*, 2015, **1**, e1500425.
34 C. Zeng, C. Liu, Y. Chen, N. L. Rosi and R. Jin, *J. Am. Chem. Soc.*, 2016, **138**, 8710–8713.
35 P. D. Jadzinsky, G. Calero, C. J. Ackerson, D. A. Bushnell and R. D. Kornberg, *Science*, 2007, **318**, 430–433.
36 Y. Chen, C. Zeng, C. Liu, K. Kirschbaum, C. Gayathri, R. R. Gil, N. L. Rosi and R. Jin, *J. Am. Chem. Soc.*, 2015, **137**, 10076–10079.
37 A. Dass, S. Theivendran, P. R. Nimmala, C. Kumara, V. R. Jupally, A. Fortunelli, L. Sementa, G. Barcaro, X. Zuo and B. C. Noll, *J. Am. Chem. Soc.*, 2015, **137**, 4610–4613.
38 C. Zeng, Y. Chen, K. Kirschbaum, K. Appavoo, M. Y. Sfeir and R. Jin, *Sci. Adv.*, 2015, **1**, e1500045.
39 P. Maksymovych, D. C. Sorescu and J. T. Yates Jr., *Phys. Rev. Lett.*, 2006, **97**, 146103.
40 A. Cossaro, R. Mazzarello, R. Rousseau, L. Casalis, A. Verdini, A. Kohlmeyer, L. Floreano, S. Scandolo, A. Morgante and M. Klein, *Science*, 2008, **321**, 943–946.

41 H. Grönbeck, H. Häkkinen and R. L. Whetten, *J. Phys. Chem. C*, 2008, **112**, 15940–15942.

42 D. E. Jiang, M. L. Tiago, W. Luo and S. Dai, *J. Am. Chem. Soc.*, 2008, **130**, 2777–2779.

43 J. Akola, M. Walter, R. L. Whetten, H. Häkkinen and H. Grönbeck, *J. Am. Chem. Soc.*, 2008, **130**, 3756–3757.

44 Y. Pei, Y. Gao and X. C. Zeng, *J. Am. Chem. Soc.*, 2008, **130**, 7830–7832.

45 O. Lopez-Acevedo, H. Tsunoyama, T. Tsukuda and C. M. Aikens, *J. Am. Chem. Soc.*, 2010, **132**, 8210–8218.

46 D. E. Jiang, *Nanoscale*, 2013, **5**, 7149–7160.

47 S. Knoppe, S. Malola, L. Lehtovaara, T. Burgi and H. Hakkinen, *J. Phys. Chem. A*, 2013, **117**, 10526–10533.

48 F. Demir and G. Kirczenow, *J. Chem. Phys.*, 2011, **134**, 121103.

49 F. Demir and G. Kirczenow, *J. Chem. Phys.*, 2012, **136**, 014703.

50 W. W. Xu, Y. Li, Y. Gao and X. C. Zeng, *Nanoscale*, 2016, **8**, 1299–1304.

51 C. Zeng, Y. Chen, K. Iida, K. Nobusada, K. Kirschbaum, K. J. Lambright and R. Jin, *J. Am. Chem. Soc.*, 2016, **138**, 3950–3953.

52 A. S. Barnard and L. A. Curtiss, *ChemPhysChem*, 2006, **7**, 1544–1553.

53 K. M. Jensen, P. Juhas, M. A. Tofanelli, C. L. Heinecke, G. Vaughan, C. J. Ackerson and S. J. Billinge, *Nat. Commun.*, 2016, **7**, 11859.

54 O. Lopez-Acevedo, J. Akola, R. L. Whetten, H. Grönbeck and H. Häkkinen, *J. Phys. Chem. C*, 2009, **113**, 5035–5038.

55 G. Kresse and J. Furthmüller, *Phys. Rev. B: Condens. Matter*, 1996, **54**, 11169–11186.

56 P. E. Blöchl, *Phys. Rev. B: Condens. Matter*, 1994, **50**, 17953–17979.

57 J. P. Perdew, K. Burke and M. Ernzerhof, *Phys. Rev. Lett.*, 1996, **77**, 3865–3868.

58 W. Tang, E. Sanville and G. Henkelman, *J. Phys.: Condens. Matter*, 2009, **21**, 084204.

59 S. Grimme, J. Antony, S. Ehrlich and H. Krieg, *J. Chem. Phys.*, 2010, **132**, 154104.

60 D. Grumelli, F. L. Maza, K. Kern, R. C. Salvarezza and P. Carro, *J. Phys. Chem. C*, 2016, **120**, 291–296.